PROCEEDINGS, 51st Workshop on Geothermal Reservoir Engineering
Stanford University, Stanford, California, February 9-11, 2026
SGP-TR-230

Thermal Gradient Signatures of Fault-Controlled Hydrothermal Systems: Insights from Conceptual Models and Field Data

Fangning Zheng, Robin Thibaut, Zhouji Liang, Junjie Yu and Ahinoam Pollack

fangning@zanskar.us

Keywords: Fault-hosted geothermal modeling, Geothermal exploration

ABSTRACT

Geothermal exploration in structurally controlled systems requires careful assessment of well placement relative to permeable fault zones and associated upflows. This study investigates multiple drilling scenarios that reflect different locations of temperature gradient holes (TGH) with respect to a fault-hosted hydrothermal reservoir and its upflow plume. Using a combination of conceptual models and field data, we compare thermal profiles from wells that (1) completely miss the reservoir, (2) encounter distal upflow from the heat source, (3) intersect the isothermal reservoir, and (4) capture shallow or proximal upflow at varying locations. We also evaluate these scenarios under different fault dip angles and rock thermal conductivities. The comparative analysis highlights diagnostic temperature-depth trends, including shallow isothermal zones, steep conductive gradients, and deep upflow signals. By integrating field observations with modeled profiles, we demonstrate how variations in well location influence both the apparent subsurface temperature structure and the inferred reservoir potential. These findings provide practical guidance for geothermal exploration strategies, emphasizing the importance of structural context, hydrothermal upflow geometry, and well trajectory when targeting economically viable resources.

1. INTRODUCTION

The geothermal systems for primary resource base power generation can be categorized mainly into hydrothermal systems and enhanced geothermal systems (EGS). Hydrothermal systems are geothermal resources that have both high temperature and high permeability rocks to produce heat for power generation. The 2008 USGS assessment of moderate- and high-temperature geothermal resources in the western United States estimated a mean power production potential of approximately 9 GWe from identified hydrothermal systems and about 30 GWe from undiscovered hydrothermal systems (Dobson, 2016). The discovery of new commercial-grade geothermal systems in the western United States is challenging because most resources are blind (Faulds et al., 2021). These blind systems lack surface manifestations such as hot springs or geysers, eliminating many of the traditional indicators used in geothermal exploration. As a result, identifying blind geothermal resources requires the integration of multiple favorable indicators, including geological factors (e.g., structural geology mapping), borehole data (temperature, pressure and spinner well logs), geophysical data (e.g., gravity, magnetotelluric, and HeliTEM resistivity surveys), and geochemical evidence (e.g., hydrothermal alteration and geothermal fluid analyses).

Heat-flow anomalies identified from temperature-gradient (TG) wells are one of the primary methods used to detect blind geothermal resources. Temperature logs from conventional exploration wells, typically drilled to depths of approximately 100–2000 ft, provide critical information for identifying upflow zones—areas characterized by high thermal potential and permeability that are suitable for geothermal development (Syabi et al., 2017). These data also help define the geometry of upflow zones along fault systems and support the construction of regional temperature-anomaly maps for blind hydrothermal exploration. The 2-m TG well systems consist of shallow wells drilled to a depth of only 2 meters for identifying blind hydrothermal systems. These wells are low cost and easy to deploy in the field, and they are effective for quantifying near-surface temperature anomalies and constructing regional heat-flow maps, such as those developed at Desert Peak, Nevada (Coolbaugh et al., 2007). However, a well depth of only 2 meters is too shallow to capture complex geological structures, and results derived from such data are often insufficient for accurately delineating deep heat sources and hydrothermal flow paths, particularly in fault-controlled hydrothermal upflow systems. The deep TG wells can provide valuable subsurface characterization of structural and depositional features, such as the location and dip direction of fault zones, particularly when combining data from multiple TG wells, image logs, and other wellbore measurements.

In addition to a heat source, a permeable pathway that enables convective fluid flow from deep reservoirs to shallower layers is essential for commercial heat production in conventional hydrothermal systems, and this pathway is most commonly provided by fault systems. Structural geology plays a critical role in identifying fault systems that can act as conduits for heat and fluid flow relevant to geothermal production. Faulds and Hinz (2015) identified eight structural settings for geothermal systems in the Great Basin region of the western United States based on an analysis of 426 known hydrothermal systems. Among these, step-overs or relay ramps within normal fault zones represent the most favorable structural setting for geothermal development. Beyond fault geometry, fault permeability and geomechanical properties are also key factors in evaluating a geothermal field. Fault permeability governs the efficiency with which hot fluids are transported from deep heat sources to shallower reservoirs, while geomechanical properties, such as Young's modulus, Poisson's ratio, friction angle, and cohesion, control whether faults remain open, undergo closure, or experience micro-seismic events during production and injection operations (Talukdar et al., 2025; Jahnke et al., 2023). These fault-related properties and events can significantly impact geothermal production performance.

Temperature profiles from TG wells drilled during exploration are among the most direct and informative indicators for identifying heat-flow anomalies and permeable pathways. The resulting temperature profiles and the broader temperature field of a geothermal site are

controlled by factors such as fault geometry (e.g., strike and dip), fault interactions, permeability, and rock and fluid properties, including porosity, thermal conductivity, and heat capacity. The shape and signature of these temperature profiles can therefore reveal the location of permeable pathways and fault structures, providing insight into the origin and transport of heat from deep reservoirs. This information is critical for decision-making related to the placement of subsequent exploration and production wells. To further quantify reservoir parameters, inverse modeling is commonly performed using reservoir simulations to match field observations, typically under geological uncertainty. In this study, we investigate the effects of fault geometry and rock properties (specifically thermal conductivity) on TG well temperature profiles, demonstrating how these profiles can be interpreted to develop an integrated understanding of fault-controlled heat-flow systems and fault-influenced heat-plume geometry, identify deep heat sources, and guide the selection of future drilling targets.

In this paper, we examine two key parameters that influence heat-plume geometry: fault dip angle and rock thermal conductivity. A 3D coupled hydro-thermal simulation model is developed and implemented, and sensitivity analyses are performed to evaluate the effects of varying fault dip angles and thermal conductivity on heat-plume evolution along a single permeable fault system. Temperature profiles from wells at different locations are analyzed under multiple scenarios (**Figure 1**), including wells that (1) miss the fault-hosted reservoir, (2) encounter shallow upflow from the heat source, (3) encounter deep upflow near the fault-hosted reservoir, (4) intersect a fault-hosted reservoir, (5) are proximal to upflow, and (6) miss the upflow. Other reservoir parameters are beyond the scope of this study and will be addressed in future work. In addition, a field case study from the Big Blind geothermal prospect in the Lone Mountain area of Nevada is used to demonstrate how core well temperature profiles can be interpreted to describe and constrain the heat source and its heat-flow evolution.

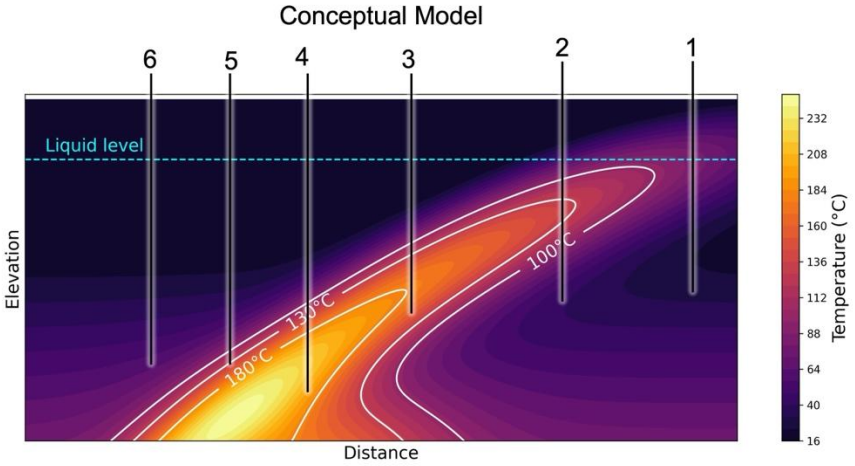

Figure 1. Conceptual model showing a fault-controlled hydrothermal upflow reservoir. Five well scenarios are shown in which the well (1) miss the fault-hosted reservoir, (2) encounter shallow upflow from the heat source, (3) encounter deep upflow near the fault-hosted reservoir, (4) intersect a fault-hosted reservoir, (5) are proximal to upflow, and (6) miss the upflow.

2. METHODOLOGY

In this section, we describe the coupled hydrothermal 3D simulation model and employed for both the sensitivity analysis and the field-scale case studies. The model is based on a real geothermal development site, the Big Blind field in Lone Mountain, Nevada. The computational domain spans approximately 19 km × 16 km × 4.2 km in the x-, y-, and z-directions, respectively. The model mesh, shown in **Figure 2**, has a maximum element size of 500 m and a minimum element size of several tens of meters. A fault is explicitly represented near the center of the domain, striking 0° (north–south) and extending approximately 3000 m to the south. The matrix is assumed to consist of a homogeneous rock type, with material properties listed in **Table 1**.

The model domain extends vertically from the basement to the water table, meaning the unsaturated zone is not explicitly simulated. At the top boundary (the water table), we apply a constant pressure Dirichlet condition of $p = 0$ (gauge pressure). Thermally, this boundary employs a Robin (mixed) condition defined as $q = h(T - T_{air})$, where h is an effective heat transfer coefficient set to $h = 50\ Wm^{-2}K^{-1}$ and T_{air} is the mean annual air temperature. This coefficient represents the lumped thermal resistance of the unmodeled vadose zone and surface exchange, a simplified approach appropriate for the shallow water tables typical of Basin and Range valleys. Consequently, the actual heat flux across the top boundary is a calculated model output determined by the temperature solution. Along the four lateral boundaries, constant hydraulic head conditions are applied, paired with open thermal boundaries that allow for both advective and diffusive heat transport. Finally, a no-flow hydraulic condition and a specified constant heat flux are imposed at the bottom boundary.

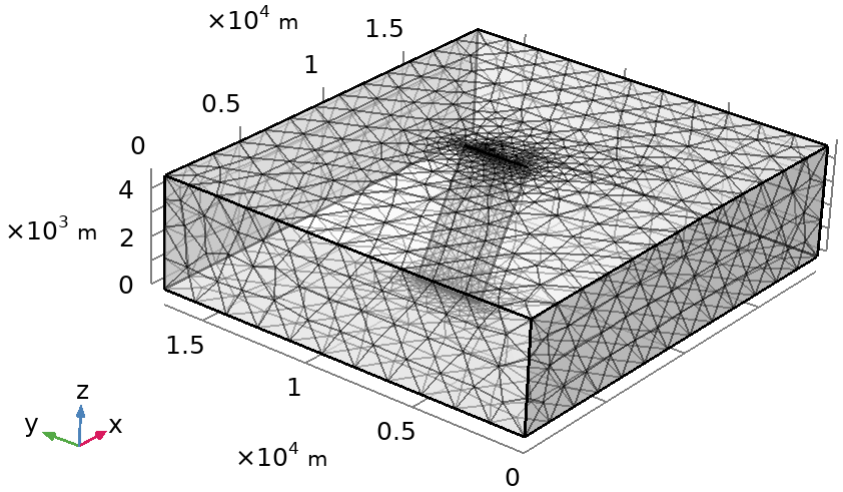

Figure 2. Simulation model mesh grid with a fault dipping at 60° in the middle of the mesh.

Table 1. Rock and fault properties of the simulation model.

		unit	value
Rock Properties	Density	kg/m^3	2000
	Porosity	-	0.25
	Permeability	m^2	2.97e-15
	k_v/k_h	-	0.3
	Heat capacity	$J\ kg^{-1}\ K^{-1}$	1000.0
	Thermal conductivity	$W\ m^{-1}\ K^{-1}$	Varying at 0.5,1,3,5,7
Fault Properties	Fault maximum permeability	m^2	1e-12
	Fault minimum permeability	m^2	1e-15

In this study, we conduct a sensitivity analysis on two key parameters: the fault dipping and the thermal conductivity (λ) of the matrix. The objective is to evaluate their combined influence on subsurface temperature distributions and the resulting temperature profiles observed at wells located at varying distances from the fault. Fault dips of 30°, 45°, 60°, and 75° to the west are considered (**Figure 3**). Thermal conductivity is varied over a range of 0.5, 1, 3, 5, and 7 $W\ m^{-1}\ K^{-1}$ (García-Noval et al., 2024). A base-case scenario is defined with a fault dip angle of 60° and a thermal conductivity of 3 $W\ m^{-1}\ K^{-1}$, against which all other simulations are compared.

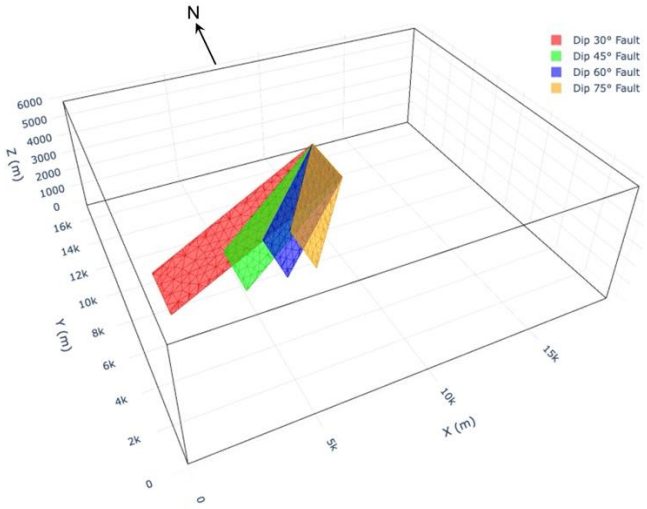

Figure 3. Fault meshes with dips of 30°, 45°, 60°, and 75° within the 3D model domain.

3. RESULTS AND DISCUSSION

In this section, we present and discuss the results of the sensitivity analysis examining the effects of fault dip angle and rock thermal conductivity. **Figure 4** illustrates the 3D temperature field of the base-case model and highlights two cross-sectional planes (the x-z and the y-z planes) used to extract the temperature distributions shown in subsequent figures. Ten wells with a depth of 2000 m are also indicated in the model. Along the x–z cross section, six wells (well 1–6) are positioned at varying distances oriented diagonally relative to the fault strike direction on the same plane. Along the y–z cross section, five wells (well 4 and well 7–10) are positioned at varying distances parallel to the fault strike direction on the same plane. Well 4 is located at the intersection of the two cross-sectional planes.

We evaluate the thermal responses at these ten well locations for the full range of fault dip angles and rock thermal conductivity values considered. The resulting temperature distributions and corresponding well temperature profiles are compared across scenarios. Finally, we present a field-scale case study, demonstrating how characteristic temperature signatures may be used to constrain fault location and dip in geothermal systems.

3.1 Varying Fault Dips

Figure 5 presents temperature cross-sectional plots and corresponding well temperature profiles for the ten well location scenarios, assuming a thermal conductivity of 3 $W\,m^{-1}\,K^{-1}$ and fault dips of 30°, 45°, 60°, and 75°. The red dashed line denotes a reference temperature threshold of 130 °C for comparison across plots. The temperature profiles represent estimated initial-state temperatures at these locations and do not account for intra-well flow between feed zones or the production of hotter fluids from greater depths that may occur after drilling or well operation. When all other reservoir parameters are held constant, increasing fault dip angle results in more efficient upward heat transport through the permeable fault zone and correspondingly higher temperatures in the overlying reservoir.

For a dip angle of 30°, the temperature field largely follows the background geothermal gradient imposed by the basal heat source. In this case, the fault does not facilitate sufficient upward heat transport to generate a distinct shallow upflow zone because the low dip angle limits the vertical component of buoyancy-driven flow along the fault. As a result, the temperature profiles for the ten wells are nearly identical, with the exception of Well 6, which exhibits a slightly elevated temperature at approximately 800 m depth. However, the magnitude of this anomaly is insufficient to support commercial geothermal development.

At a dip angle of 45°, a weak thermal upflow zone becomes apparent in the cross-sectional temperature plots. This upflow marginally approaches the commercial geothermal threshold temperature (~130 °C) at a depth of approximately 2000 m, indicating limited enhancement of heat transport relative to the lower dip case.

For a dip angle of 60°, a pronounced thermal upflow zone is clearly observed in the temperature field, with several wells reaching commercially viable temperatures at substantially shallower depths. In this scenario, Well 1 corresponds to case (1) in **Figure 1**, in which the well does not intersect the thermal system. Well 2 encounters a shallow upflow, reaching a temperature of approximately 100 °C at a depth of ~300 m. Wells 3 and 4 intersect a deeper upflow zone near the reservoir, characterized by steep temperature gradients at shallow depths that transition to near-constant profiles below the upflow. Well 5 intersects an isothermal reservoir region with temperatures exceeding the commercial threshold. In contrast, Well 6 exhibits a nearly linear temperature profile with an approximately constant geothermal gradient, suggesting that the well is located proximal to, but does not directly intersect, the primary upflow zone.

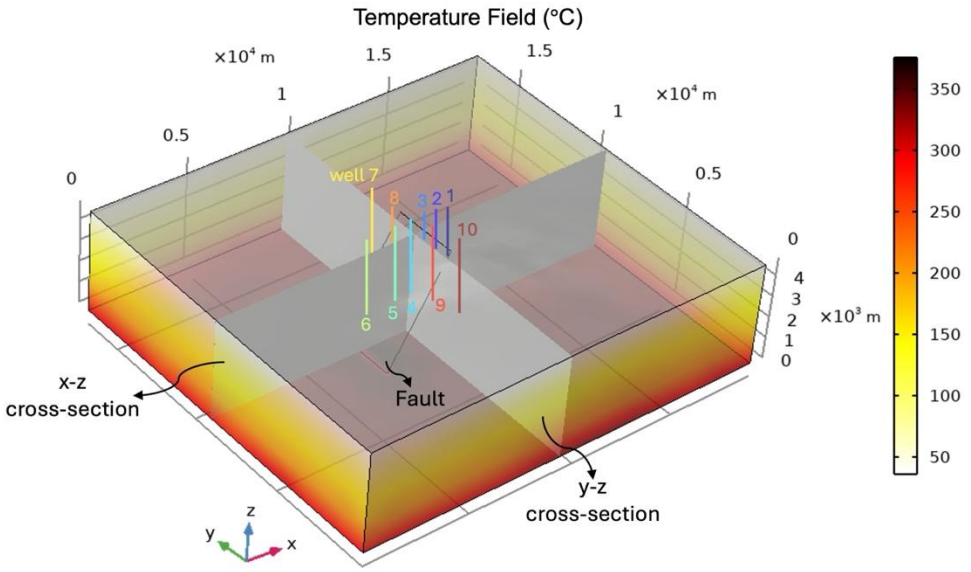

Figure 4. Temperature field of the 3D model with two cross-sectional planes (grey x-z and y-z planes) to show the temperature cross-sectional plots. Ten different well locations are also shown on the model that are aligned along the two cross-sectional planes.

For a fault dip angle of 75°, the thermal upflow along the fault becomes both more pronounced and higher in temperature. Although Well 1 slightly misses the primary upflow zone, it exhibits a higher temperature gradient than in the lower dip-angle cases. Wells 2 and 3 intersect the upflow zone and encounter shallow thermal anomalies at depths of approximately 500 m, where temperatures reach about 130 °C. Wells 4, 5, and 6 display nearly linear temperature profiles, with temperatures exceeding 130 °C at greater depths of approximately 1000 m, 1300 m, and 1800 m, respectively.

Figure 6 illustrates well-by-well temperature–depth profiles for fault dip angles of 30°, 45°, 60°, and 75°, assuming a rock thermal conductivity of 3 $W\,m^{-1}\,K^{-1}$. For reference, the vertical dashed line denotes the approximate commercial geothermal threshold temperature of 130 °C. Overall, increasing fault dip angle systematically enhances upward heat transport, resulting in higher temperatures at shallower depths across most well locations.

At Well 1, temperature profiles primarily reflect background conductive gradients for dip angles up to 60°, while the 75° case exhibits a noticeably steeper gradient, indicating proximity to enhanced heat transfer along the fault despite not directly intersecting the primary upflow zone. Wells 2 and 3 show progressively stronger deviations from the conductive background with increasing dip angle, transitioning from near-linear profiles at low dip angles to pronounced shallow thermal anomalies for dip angles of 60° and 75°, consistent with direct intersection of the fault-controlled upflow zone.

Wells 4 and 5 display relatively linear temperature profiles for lower dip but develop elevated temperatures at intermediate depths as dip angle increases, with temperatures exceeding 130 °C at progressively shallower depths for steeper faults. These profiles suggest indirect or partial intersection with the upflow zone, where advective heat transport augments the conductive background.

Collectively, the well-specific comparisons demonstrate that fault dip angle exerts a strong control on both the magnitude and depth distribution of reservoir temperatures. Steeper faults promote more efficient vertical heat transport, increasing the likelihood of encountering commercially viable temperatures at shallower depths, while lower dip angles result in temperature profiles dominated by the regional geothermal gradient. Over longer timescales in older geothermal systems, however, shallower-angle faults may promote the development of a more laterally extensive heated rock matrix.

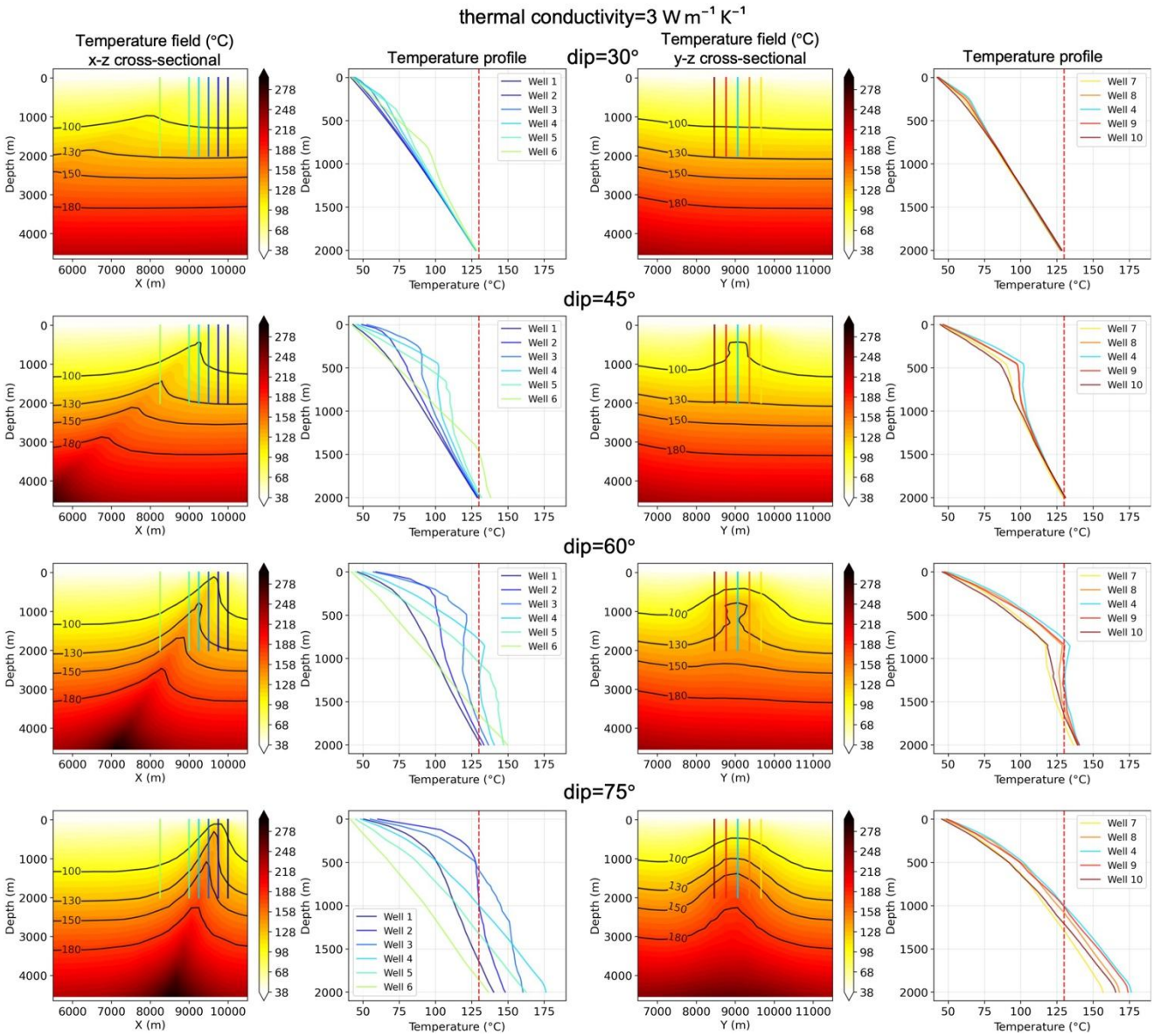

Figure 5. Temperature cross-sectional plots and well profiles for the ten well scenarios under thermal conductivity of 3 $W\ m^{-1}\ K^{-1}$ and varying fault dip angle of 30°, 45°, 60°, and 75°. The red dashed line indicates a reference 130 °C commercial temperature threshold.

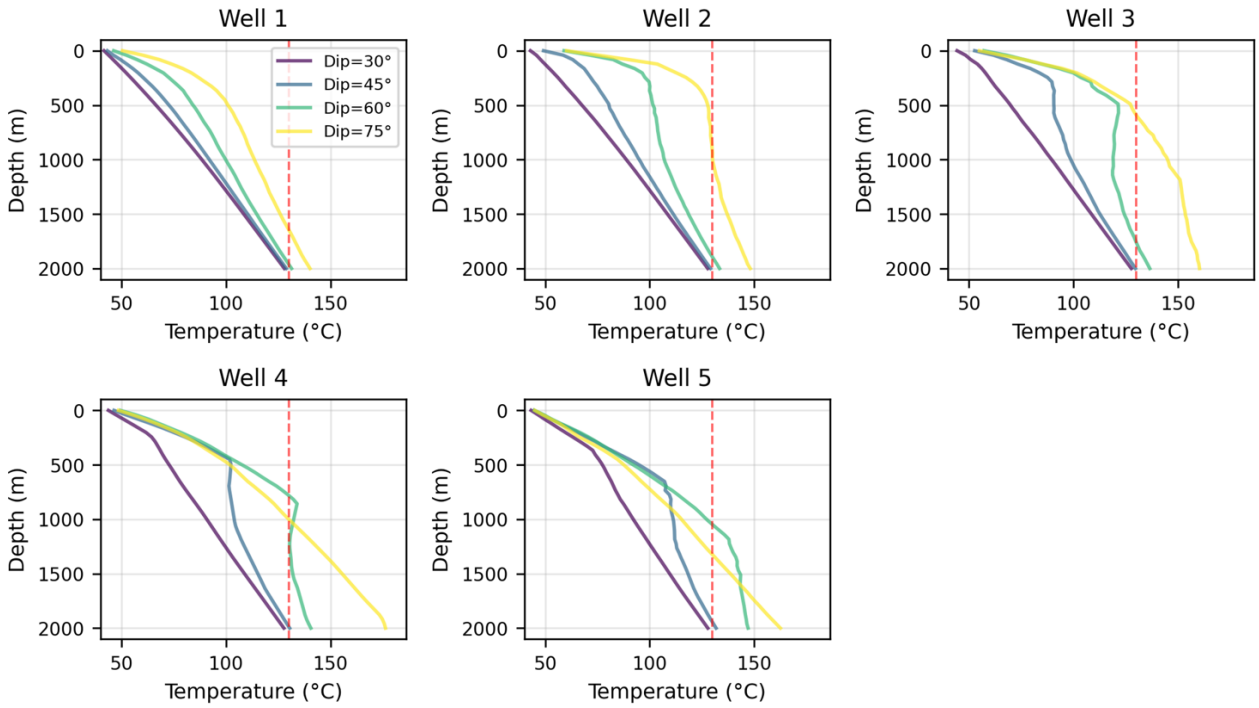

Figure 6. Comparison of temperature profiles at individual well locations for varying fault dip angles. The red dashed line indicates a reference 130 °C commercial temperature threshold.

3.2 Varying Rock Thermal Conductivity

Figure 7 shows temperature distributions and corresponding well temperature profiles for a range of rock thermal conductivity values (λ =1, 3, 5, and 7 $W\ m^{-1}\ K^{-1}$) and a fault dip angle of 60°. For each thermal conductivity case, results are shown for both the x–z and y–z cross sections. In each row, the left panels display cross-sectional temperature fields with isotherms, while the adjacent panels show temperature–depth profiles for wells intersecting the respective cross sections. Vertical colored lines in the cross-sectional plots indicate well locations, and the vertical dashed line in the profile plots marks the approximate commercial geothermal threshold temperature of 130 °C for comparison purpose only and not implying producibility.

For low thermal conductivity ($\lambda = 1\ W\ m^{-1}\ K^{-1}$), strong thermal anomalies are observed along the fault zone in both cross sections, characterized by closely spaced isotherms and elevated temperatures extending to shallow depths. Corresponding well temperature profiles exhibit pronounced curvature and localized temperature maxima, indicating strong thermal retention and enhanced influence of convective heat transport near the fault. Several wells reach or exceed the commercial temperature threshold at relatively shallow depths.

As thermal conductivity increases to $\lambda = 3$ and 5 $W\ m^{-1}\ K^{-1}$, the amplitude of the thermal anomaly decreases and the isotherms become more laterally uniform. Temperature profiles for individual wells shift toward lower temperatures at a given depth. Wells still influenced by the fault exhibit elevated temperatures relative to the background geothermal gradient, but peak temperatures occur at greater depths.

At the highest thermal conductivity ($\lambda = 7\ W\ m^{-1}\ K^{-1}$), the temperature field is largely dominated by conductive heat transfer. Isotherms are smoother and more evenly spaced, and fault-related thermal anomalies are significantly attenuated. Corresponding well temperature profiles are nearly linear and closely clustered, with most wells intersecting the commercial temperature threshold only at greater depths or not at all.

Overall, the figure demonstrates that increasing rock thermal conductivity leads to more efficient heat dissipation, reduced thermal retention of the reservoir rocks, and lower reservoir temperatures at shallow to intermediate depths. These results highlight the strong control of thermal conductivity on the expression of fault-related thermal anomalies and the depth at which commercially viable temperatures may be encountered in younger geothermal systems where the geothermal anomaly has not had sufficient time to propagate upwards..

The systematic decrease in temperature with increasing thermal conductivity reflects the enhanced efficiency of conductive heat dissipation. Under the imposed basal heat-flux boundary condition, heat transfer is governed by Fourier's law of heat conduction:

$$q = -\lambda \frac{dT}{dz} \tag{1}$$

Where q represents the heat flux, λ is thermal conductivity, $\frac{dT}{dz}$ is the geothermal gradient. In the model, a constant heat-flux boundary condition over time is applied at the base of the domain, while open boundary conditions are prescribed along the four lateral boundaries (between models with different thermal conductivities, the heat flux is increased in proportion to the thermal conductivity). For a fixed basal heat flux, higher thermal conductivity results in a reduced vertical temperature gradient, leading to lower temperatures at shallow and intermediate depths. In addition, increased thermal conductivity enhances both lateral and vertical redistribution of heat away from fault-controlled upflow zones, thereby attenuating localized thermal anomalies. Consequently, at younger geothermal systems, low-conductivity systems promote heat retention and elevated reservoir temperatures, whereas high-conductivity systems favor thermal smoothing and reduced geothermal potential at accessible depths. In older geothermal systems, longer timescales allow heat from depth to propagate upward, making higher thermal conductivity more favorable, as a larger volume of host rock surrounding fault zones becomes heated and a smaller fraction of heat is lost through surface manifestations. Higher thermal conductivity, combined with a larger volume of heated rock matrix, would also help reduce thermal breakthrough in these fault-dominated systems.

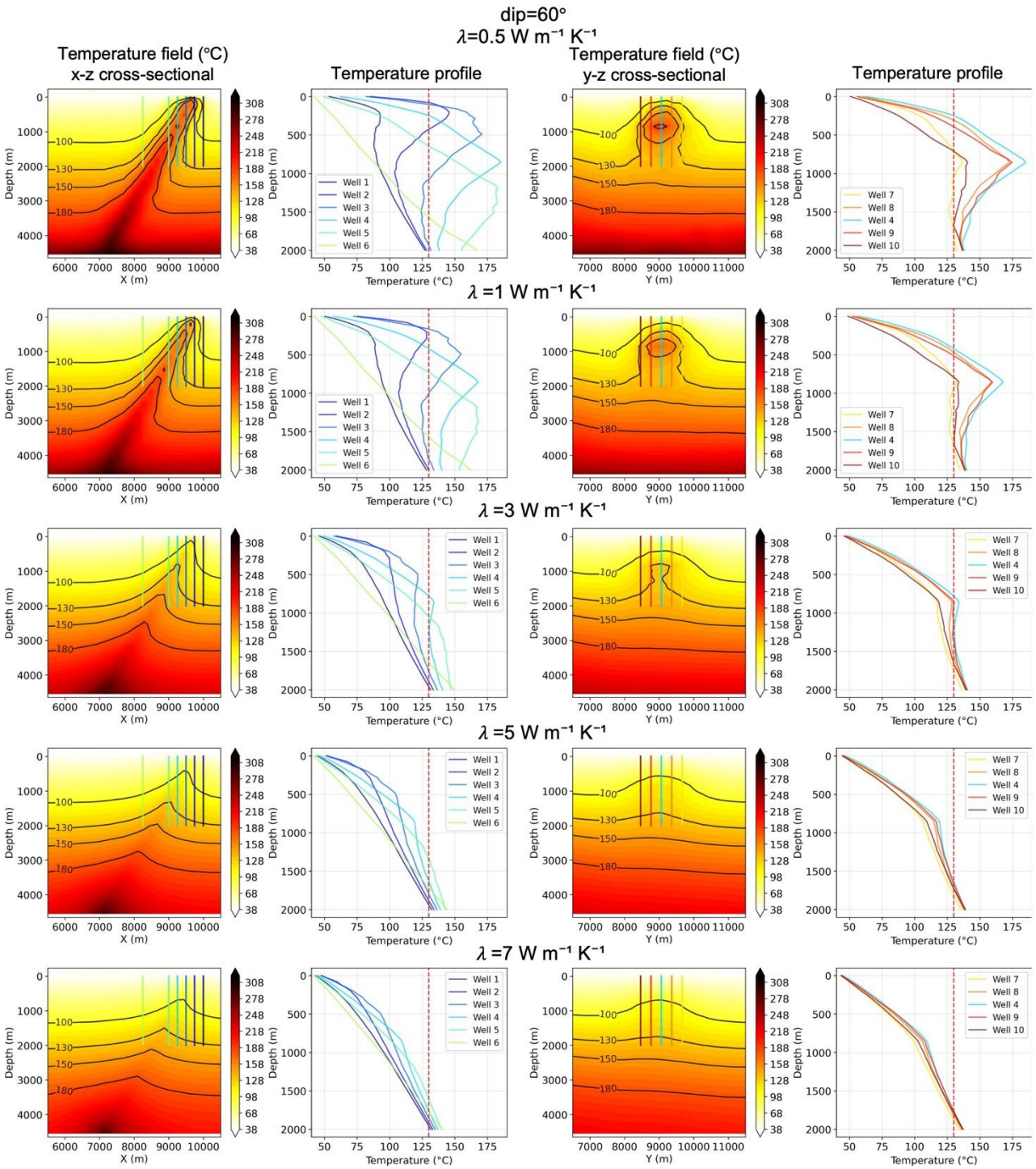

Figure 7. Temperature cross-sectional plots and well profiles for the ten well scenarios under fault dip of 60° and varying thermal conductivity of 0.5, 1, 3, 5, 7 $W\ m^{-1}\ K^{-1}$. The red dashed line indicates a reference 130 °C commercial temperature threshold.

Figure 8 presents temperature–depth profiles for five wells under varying rock thermal conductivity values (λ = 0.5, 1, 3, 5, and 7 $W\ m^{-1}\ K^{-1}$), while all other model parameters are held constant. The vertical dashed line indicates the approximate commercial geothermal threshold temperature of 130 °C. Across all wells, increasing thermal conductivity leads to systematically lower temperatures at a given depth.

At Wells 1 and 2, temperature profiles remain largely linear at depth but exhibit localized curvature at shallow depths for lower thermal conductivity cases, indicating enhanced thermal retention near the heat source or fault-controlled upflow zones. Wells 3–5 display more pronounced thermal anomalies at intermediate depths for low thermal conductivity values, whereas these anomalies diminish progressively as thermal conductivity increases.

Overall, the well-by-well comparison demonstrates that under the thermal boundary conditions described in the Methodology section (open boundary on the side walls and constant heat flux on the bottom), rock thermal conductivity exerts a strong control on the amplitude of subsurface temperatures, with lower thermal conductivity favoring faster propagation of geothermal heat anomalies, but also limiting the lateral size of the geothermal plume in the long run.

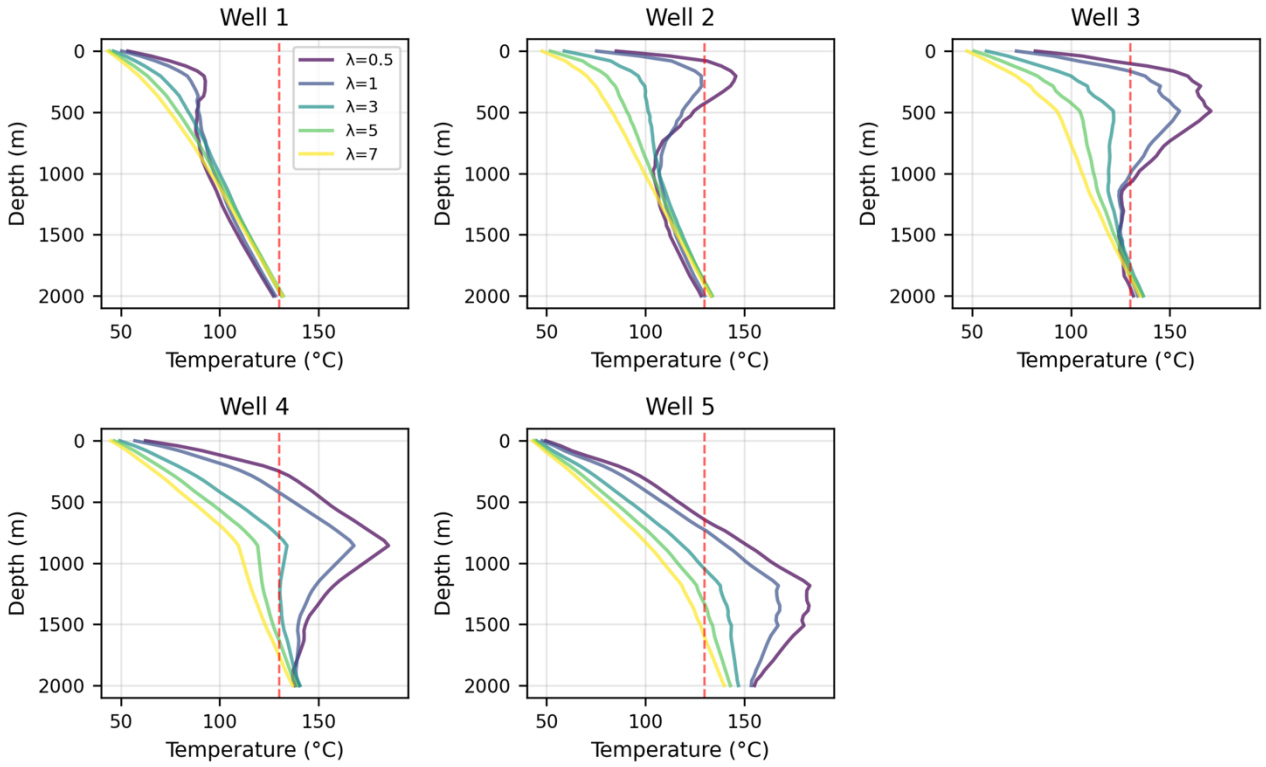

Figure 8. Comparison of temperature profiles at individual well locations for varying rock thermal conductivity (λ). The red dashed line indicates a reference 130 °C commercial temperature threshold.

3.3 Case Study: Big Blind, Lone Mountain, NV

Big Blind is a geothermal discovery site located in Lone Mountain, Nevada, where multiple high-resolution geophysical datasets, including gravity and magnetotelluric (MT) surveys, have been acquired. Shallow exploration wells were initially drilled, followed by two deeper core wells with total depths of approximately 800 m. The observed temperature logs from these wells are shown in **Fig. 10**. Well A intersects a shallow thermal upflow at a depth of approximately 80 m, where temperatures reach about 75 °C and remain nearly constant down to 800 m. In contrast, Well B exhibits a linear temperature profile characterized by a constant geothermal gradient over the entire depth interval.

Based on the observed temperature data and the geological constraints of the site, we develop a three-dimensional reservoir simulation model to history match the temperature profiles of the two wells. The computational mesh of the 3D model is shown in **Figure 9** with fault geometries. The model settings follow those described in the Methodology section, with the only exception of the fault geometry.

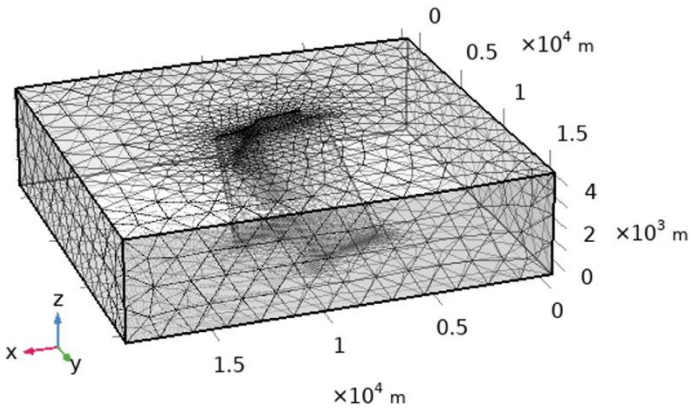

Figure 9. The computational mesh of the 3D model for Big Blind site with faults geometries.

The optimized 3D model is shown in **Fig. 11a**, which presents the modeled temperature field of the 85 °C isotherm and the fault geometry. **Figure 11b** provides a zoomed-in view of **Fig. 11a**, highlighting the 85 °C isotherm in greater detail. The results indicate the development of a fault-controlled thermal upflow along the fault zone in the vicinity of Wells A and B.

The simulated temperature profiles for both wells are shown in **Fig. 10** (red curves). In this configuration, Well A does not intersect the primary upflow zone, resembling the Well 1 scenario identified in the sensitivity analysis, in which a low temperature upflow is encountered at shallow depth. In contrast, Well B is located proximal to the upflow zone, analogous to the Well 5 scenario from the sensitivity cases, and exhibits a nearly linear temperature profile. The simulated temperature profiles successfully reproduce the characteristic temperature signatures observed for these two well configurations.

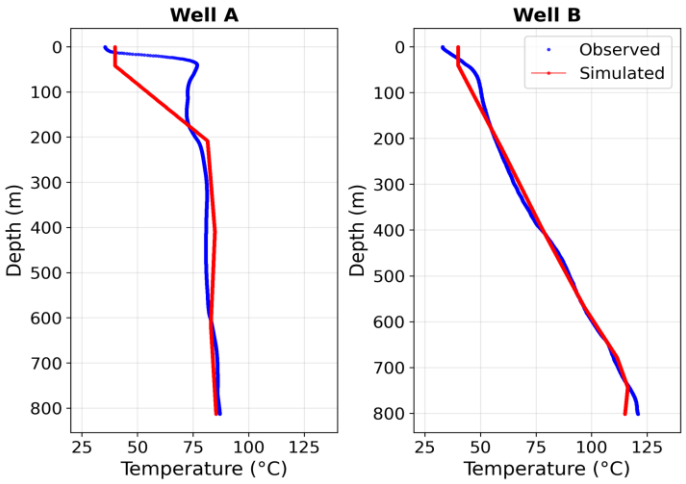

Figure 10. The observed (blue) and the simulated (red) temperature profile of well A and well B.

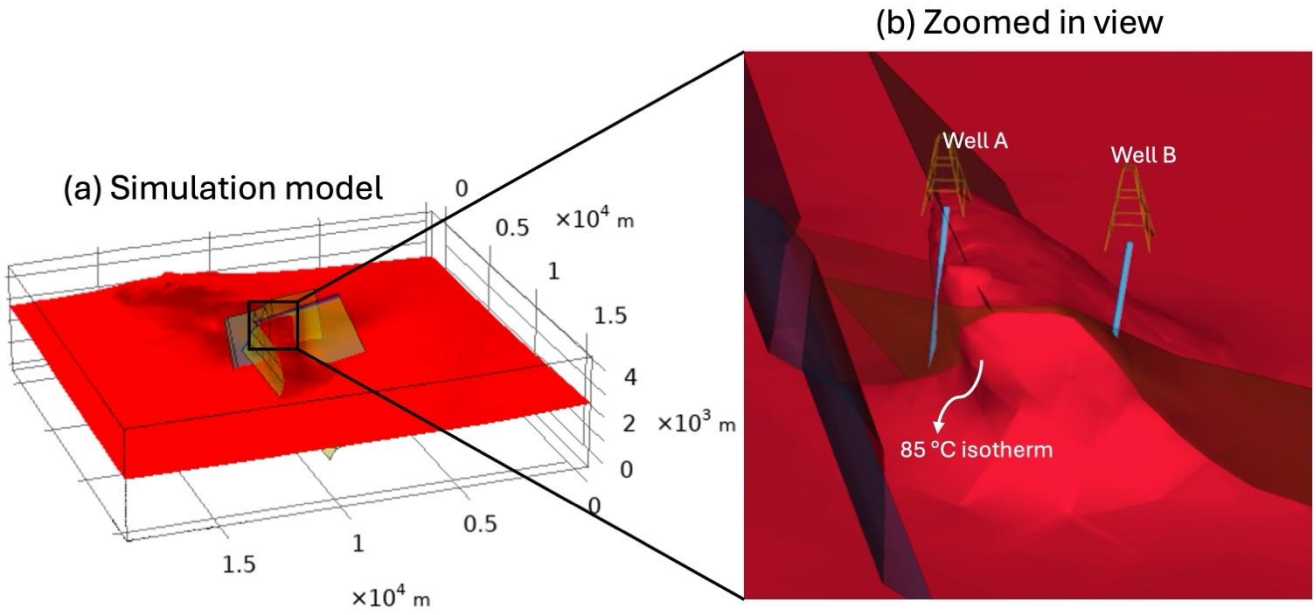

Figure 11. (a) History-matched simulation results showing the modeled temperature field with the 85 °C isotherm and the fault geometry. (b) Zoomed-in view of panel (a) highlighting the 85 °C isotherm. A fault-controlled thermal upflow develops along the fault zone in the vicinity of Wells A and B. In this configuration, Well A does not intersect the primary upflow zone, whereas Well B is located proximal to the upflow zone.

CONCLUSION

This study evaluates the effects of fault dip and rock thermal conductivity on subsurface temperature distributions and well temperature signatures in fault-controlled geothermal systems using a three-dimensional thermal–hydraulic model. Sensitivity analyses show that fault dip angle strongly controls vertical heat transport, with steeper faults producing more pronounced thermal upflow zones and higher temperatures at shallower depths. In contrast, low-angle faults yield temperature profiles dominated by conductive heat transfer with limited shallow thermal anomalies. Rock thermal conductivity plays a key role in controlling reservoir temperatures. Under a fixed basal heat-flux boundary condition, higher thermal conductivity enhances heat dissipation, reduces temperature gradients, and weakens fault-related thermal anomalies, shifting commercially viable temperatures to greater depths. Lower thermal conductivity favors heat retention close to the fault and elevated reservoir temperatures. Over longer timescales in older geothermal systems, however, shallower-angle faults and higher thermal conductivities would promote the development of a more laterally extensive heated rock matrix.

Application of the modeling framework to the Big Blind geothermal discovery site in Lone Mountain, Nevada, demonstrates the practical utility of the sensitivity results. History matching of observed temperature logs from two wells reproduces contrasting thermal signatures consistent with the sensitivity scenarios: one well missing the primary upflow zone and another located proximal to it. The agreement between modeled and observed temperature profiles supports the interpretation of a fault-controlled thermal system and illustrates how temperature signatures can be used to constrain fault location and geometry in early-stage geothermal exploration.

Overall, this study highlights the importance of integrating fault geometry, thermal properties, and well temperature data when assessing geothermal potential. The results provide a physically based framework for interpreting temperature logs, guiding well placement, and reducing exploration risk in structurally controlled geothermal systems.

REFERENCES

Burns, E.R., Williams, C.F., and DeAngelo, J., 2025, Enhanced geothermal systems electric-resource assessment for the Great Basin, southwestern United States: U.S. Geological Survey Fact Sheet 2025–3027, 4 p. https://doi.org/10.3133/fs20253027.

Coolbaugh, M.F., Sladek, C., Faulds, J.E., Zehner, R.E. and Oppliger, G.L., 2007, January. Use of rapid temperature measurements at a 2-meter depth to augment deeper temperature gradient drilling. In Proceedings, thirty-second workshop on geothermal reservoir engineering, Stanford University (Vol. 8).

Dobson, P.F., 2016. A review of exploration methods for discovering hidden geothermal systems. GRC Transactions, 40, pp.695-706.

Faulds, J. and Hinz, N., 2015, April. Favorable tectonic and structural settings of geothermal systems in the Great Basin region, western USA: Proxies for discovering blind geothermal systems. In Proceedings World Geothermal Congress, Melbourne, Australia, 19-25 April 2015 (No. DOE-UNR-06731-02). Nevada Bureau of Mines and Geology, University of Nevada, Reno.

Faulds, J.E., Hinz, N.H., Coolbaugh, M., Ayling, B., Glen, J., Craig, J.W., McConville, E., Siler, D., Queen, J., Witter, J. and Hardwick, C., 2021. Discovering blind geothermal systems in the Great Basin Region: An integrated geologic and geophysical approach for establishing geothermal play fairways: All phases (No. DOE-UNR-06731-01). Univ. of Nevada, Reno, NV (United States); ATLAS Geosciences, Inc., Reno, NV (United States); US Geological Survey, Menlo Park, CA (United States); Hi-Q Geophysical, Inc., Ponca City, OK (United States); Innovate Geothermal Ltd, Vancouver (Canada); Utah Geological Survey, Salt Lake City, UT (United States).

García-Noval, C., Álvarez, R., García-Cortés, S., García, C., Alberquilla, F. and Ordóñez, A., 2024. Definition of a thermal conductivity map for geothermal purposes. Geothermal Energy, 12(1), p.17.

Jahnke, B., Sone, H., Guo, H., Sherman, C., Warren, I., Kreemer, C., Thurber, C.H., Feigl, K.L. and WHOLESCALE Team, 2023. Geomechanical analysis of the geothermal reservoir at San Emidio, Nevada. Geothermics, 110, p.102683.

Siler, D.L., 2023. Structural discontinuities and their control on hydrothermal systems in the Great Basin, USA. Geoenergy, 1(1), pp.geoenergy2023-009.

Syabi, H.F., Sentosa, R.A., Ramadhan, A.G. and CSSSA, B.Y., 2017. Determining Upflow/Outflow Zone and Fluid Flow in Geothermal Prospect Area Based on Geoindicator Comparison Value: A Case Study of Mt. Telomoyo, Central Java, Indonesia.

Talukdar, M., Zheng, F. and Jha, B., 2025. Hydrogen leakage via caprock fracturing and fault reactivation during subsurface porous media storage. International Journal of Hydrogen Energy, 149, p.149786.